2013

Non-Equilibrium Pressure Control of the Height of a Large-Scale, Ground-Coupled, Rotating Fluid Column

R. L. Ash
Old Dominion University, rash@odu.edu

I. R. Zardadhkan

Follow this and additional works at: https://digitalcommons.odu.edu/mae_fac_pubs

Part of the Aerodynamics and Fluid Mechanics Commons, Engineering Mechanics Commons, and the Fluid Dynamics Commons

Non-equilibrium pressure control of the height of a large-scale, ground-coupled, rotating fluid column

R. L. Ash[1,a)] and I. R. Zardadkhan[2]
[1]*Mechanical & Aerospace Engineering Department, Old Dominion University, Norfolk, Virginia 23529, USA*
[2]*Javelin Technologies, Oakville, Ontario L6L 0C4, Canada*

When a ground-coupled, rotating fluid column is modeled incorporating non-equilibrium pressure forces in the Navier-Stokes equations, a new exact solution results. The solution has been obtained in a similar manner to the classical equilibrium solution. Unlike the infinite-height, classical solution, the non-equilibrium pressure solution yields a ground-coupled rotating fluid column of finite height. A viscous, non-equilibrium Rankine vortex velocity distribution, developed previously, was used to demonstrate how the viscous and non-equilibrium pressure gradient forces, arising in the vicinity of the velocity gradient discontinuity that is present in the classical Rankine vortex model, effectively isolate the rotating central fluid column from the outer potential vortex region. Thus, the non-equilibrium region acts to confine and shield the central, rigid-body-like, rotating fluid core, justifying this examination of how such a rotating fluid column can interact with the ground. The resulting non-equilibrium ground-coupled, rotating fluid column solution was employed to estimate the central column heights of three well-documented dust devils, and the central column height predictions were consistent with published dust devil height statistics. © *2013 AIP Publishing LLC*. [http://dx.doi.org/10.1063/1.4807068]

I. INTRODUCTION

An understanding of how an axial vortex interacts with a solid surface is of fundamental importance in the study of viscous flows. A variety of important industrial and geophysical flows can be modeled utilizing a steady-state axial vortex whose rotational axis is perpendicular to and interacting with a fixed (ground) surface. One challenge in the study of these flows is how to properly model the nearly inviscid outer axial vortex region while incorporating viscous central and ground plane interactions. Fernandez-Feria *et al.*[1,2] have been studying the behavior of high-Reynolds number boundary layers beneath nearly inviscid vortices for some time. Recently, Parras and Fernandez-Feria[2] incorporated a far-field Long's vortex model[3] with an axisymmetric Navier-Stokes numerical solver to study the influence of Reynolds number on vortex flow behavior near the ground plane. That work showed that vortex breakdown bubbles could form on the rotational axis and elsewhere within the flow volume, depending on the Reynolds number. Vortex stability and breakdown behavior have been studied extensively for decades,[4] primarily for aircraft performance and safety considerations. However, fundamental questions remain concerning the relevance of vortex breakdown phenomena in understanding the behavior of large-scale cyclonic flows.

A variety of vortex chambers have been employed to study the interaction of axial vortices with the ground.[5–9] Unfortunately, those facilities can neither reproduce the unconfined outer geophysical boundary region nor achieve the scales (and Reynolds numbers) associated with geophysical vortex flows. Church *et al.*[6] demonstrated experimentally that vortex breakdown bubbles could be created on the axis of a simulated cyclonic flow, but they ascribed the vortex breakdown to transition from a

---

a)Author to whom correspondence should be addressed. Electronic mail: RAsh@odu.edu

laminar axisymmetric core to a turbulent core, and other processes may be important in producing stagnation zones within geophysical vortices. The inviscid nature of the measured velocity profiles in dust devils and other cyclonic geophysical flows away from the rotational axis and at moderate distances above the ground[10,11] supports the assertion that a steady-state Rankine vortex model,[12] though oversimplified, is a reasonable approximation for the large-scale velocity distribution away from the ground. Interestingly, the shear discontinuity separating the rigidly rotating central fluid column from the outer potential-flow vortex in the inviscid Rankine model implies that two distinct flow regimes can be examined when this type of vortex structure interacts with the ground.

We have examined how the inclusion of non-equilibrium pressure gradient forces in the Navier-Stokes equations can influence vortex flow structure.[13–15] That research resulted in an exact solution for a steady, incompressible axial vortex that blended rigid-body rotation near the centerline with a potential vortex velocity distribution.[15] In other words, the exact solution incorporating non-equilibrium pressure gradient forces, eliminated the velocity gradient discontinuity exhibited in the inviscid Rankine vortex model, while replicating simultaneously the limiting centerline and far field velocity distributions. The exact solution demonstrated how these non-equilibrium pressure gradient forces act to balance the viscous forces that arise in the relatively thin region where the rapidly rising azimuthal velocity, required by the outer potential vortex solution, transitions to a rigidly rotating central fluid column. When the exact, non-equilibrium solution was compared with measured and observational data for aircraft wake vortices, dust devils, and tornadoes, the azimuthal velocity profile solution was found to agree with observation. Furthermore, that incompressible exact solution predicted that the pressure deficit at the center of this type of axial vortex was twice as large as the pressure deficit that occurred at the radius of maximum swirl velocity.

Non-equilibrium pressure gradient forces appear to be important only under special circumstances, and the inner region of incompressible, potential-vortex-like flow structures may be the most important flow units exhibiting significant non-equilibrium effects. While the rotating central column regions associated with wake vortices and dust devils are rather small, it is important to note that very large-scale, rigid body-like rotating atmospheric phenomena have been modeled successfully using an inviscid energy-enstrophy statistical approach,[16] and it is apparent that the mathematics describing inviscid, incompressible vortex-like flows can be utilized over very large length scales. At the smaller scales associated with terrestrial vortices, where viscous forces in simple fluids like air and water begin to assert control over the core region of an axial vortex, finite acoustic propagation speed effects can become relevant. That is, if the fluid cannot maintain thermodynamic equilibrium near the fluid rotational axis, a symptom of that non-equilibrium can be the production and radiation of sound. Such a non-equilibrium acoustic source was identified in our earlier study.[15]

II. ISOLATION OF ROTATING FLUID COLUMN AWAY FROM THE GROUND

When non-equilibrium pressure gradient forces are incorporated in the viscous model for a steady-state axial vortex with specified circulation,[15] the improved "Rankine vortex" azimuthal velocity distribution is given by the exact solution

$$v_\theta(r) = 2v_{\theta,MAX} \frac{(r/r_{core})}{(r/r_{core})^2 + 1}.$$ (1)

The maximum rotational velocity is $v_{\theta,MAX} = v_\theta(r_{core})$, and the far-field circulation is given by

$$\Gamma_\infty = 2\Gamma_{core} = 2\left(2\pi \, r_{core} v_{\theta,MAX}\right).$$ (2)

The maximum rotational velocity is related to the pressure relaxation coefficient, η_p,[13] and depends on the ratio of the kinematic viscosity to the pressure relaxation coefficient for laminar vortices, or on the ratio of the eddy viscosity to the pressure relaxation coefficient for turbulent vortices. The maximum velocity and therefore the ratio of viscosity to pressure relaxation coefficient can also be related directly to the maximum pressure deficit. Designating ambient pressure as P_∞ and the axial centerline pressure as P_{CL}, the maximum velocity is thus related to the maximum pressure deficit

$(P_\infty - P_{CL})$, as follows:

$$v_{\theta,MAX} = \sqrt{2\frac{\nu}{\eta_p}} = \sqrt{\frac{P_\infty - P_{CL}}{2\rho}}, \qquad (3)$$

where ρ is the (constant) fluid density, demonstrating that the measured maximum pressure deficit can be utilized to estimate the ratio of the viscosity parameter to the pressure relaxation coefficient.

If the velocity distribution, Eq. (1), is utilized as an improved Rankine vortex model for the steady-state aspects of large-scale geophysical vortices away from the ground, the axial component of vorticity associated with that velocity distribution varies with radial distance from the center of rotation according to

$$\frac{\pi\, r_{core}^2}{\Gamma_\infty}\omega_z(r) = \frac{\pi\, r_{core}^2}{\Gamma_\infty}\frac{1}{r}\frac{d}{dr}(r v_\theta) = \frac{1}{\left[\left(\dfrac{r}{r_{core}}\right)^2 + 1\right]^2}. \qquad (4)$$

On that basis, it can be seen that the vorticity associated with the viscous core region for this type of vortex decreases to 1% of its centerline value at a distance of three core radii from the centerline; beyond that radius, viscous and non-equilibrium effects are nearly negligible compared with the core region and the "outer" velocity profile can be approximated accurately as a potential vortex. It is also important to note that the velocity profile within the inner 10% of the core region can be represented as a rigidly rotating fluid column to within 1% accuracy, and the inner 30% of the core region rotates like a rigid fluid column to within 10% accuracy.

Our earlier axial vortex solution demonstrated that a relatively small vorticity zone could be identified, separating the outer potential vortex flow regime from the near-rigidly rotating central fluid column. Since the central fluid column regions of geophysical vortex flows can be quite large, the behavior of such a rotating fluid column element, when "shielded" from the outer flow, warranted further study. The work that follows is an examination of the influence of viscous and non-equilibrium pressure coupling on the steady-state aspects of a rotating fluid column interacting with the ground.

More than 70 years ago, Bödewadt[17] employed boundary layer-like approximations to model a steady, rotating fluid column interacting with the ground. Schlichting[18] demonstrated subsequently that Bödewadt could have utilized his similarity velocity functions in the axial component of the conservation of momentum equation to develop a height-dependent pressure correction and thus remove the simplifying approximation restrictions, producing an exact three-dimensional solution to the incompressible Navier-Stokes equations. The same approach employed by Bödewadt, as modified by Schlichting, has been utilized here to develop an exact solution for a ground-coupled, rotating fluid column, when the incompressible Navier-Stokes equations are modified to incorporate non-equilibrium pressure forces. It is important to recognize that the solution that follows has assumed that the angular rotation rate (ω) and the ambient properties of the fluid column, including the pressure relaxation coefficient, η_P, are specified constants.

III. GROUND-COUPLED ROTATING FLUID COLUMN FORMULATION

The steady, incompressible conservation of mass and momentum equations incorporating pressure relaxation[15] can be represented in cylindrical coordinates (r, θ, z, with corresponding velocity components v_r, v_θ, v_z), assuming that gravity acts in the negative z-direction, as follows:
Conservation of mass (continuity):

$$\frac{1}{r}\frac{\partial}{\partial r}(r v_r) + \frac{\partial v_z}{\partial z} = 0. \qquad (5)$$

Conservation of radial momentum:

$$v_r\frac{\partial v_r}{\partial r} + v_z\frac{\partial v_r}{\partial z} - \frac{v_\theta^2}{r} = -\frac{1}{\rho}\frac{\partial P}{\partial r} + \nu\left[\frac{\partial^2 v_r}{\partial r^2} + \frac{\partial}{\partial r}\left(\frac{v_r}{r}\right) + \frac{\partial^2 v_r}{\partial z^2}\right] + \frac{\eta_p}{\rho}\left[v_r\frac{\partial^2 P}{\partial r^2} + v_z\frac{\partial^2 P}{\partial z\,\partial r}\right]. \qquad (6)$$

Conservation of azimuthal momentum:

$$v_r \frac{\partial v_\theta}{\partial r} + v_z \frac{\partial v_\theta}{\partial z} + \frac{v_r v_\theta}{r} = \nu \left[\frac{\partial^2 v_\theta}{\partial r^2} + \frac{\partial}{\partial r} \left(\frac{v_\theta}{r} \right) + \frac{\partial^2 v_\theta}{\partial z^2} \right] + \frac{\eta_p}{\rho} \frac{v_\theta}{r} \frac{\partial P}{\partial r}. \tag{7}$$

Conservation of axial momentum:

$$v_r \frac{\partial v_z}{\partial r} + v_z \frac{\partial v_z}{\partial z} = -g - \frac{1}{\rho} \frac{\partial P}{\partial z} + \nu \left[\frac{1}{r} \frac{\partial}{\partial r} \left(r \frac{\partial v_z}{\partial r} \right) + \frac{\partial^2 v_z}{\partial z^2} \right] + \frac{\eta_p}{\rho} \left[v_r \frac{\partial^2 P}{\partial r \partial z} + v_z \frac{\partial^2 P}{\partial z^2} \right]. \tag{8}$$

Note that the $\frac{\eta_p}{\rho}$ prefix precedes the non-equilibrium pressure terms in the three components of the conservation of momentum equation.

Utilizing the Bödewadt transformations,[17]

$$\varsigma = z \sqrt{\frac{\omega}{\nu}}, \quad \text{with } v_r = r \omega F(\varsigma), \quad v_\theta = r \omega G(\varsigma), \quad \text{and } v_z = \sqrt{\nu \omega} H(\varsigma), \tag{9}$$

the transformed conservation equations are
Continuity:

$$2F + \frac{dH}{d\varsigma} = 0. \tag{10}$$

Conservation of radial momentum:

$$F^2 + H \frac{dF}{d\varsigma} - G^2 = -\frac{1}{r\omega^2} \left[\frac{1}{\rho} \frac{\partial P}{\partial r} \right] + \eta_p \omega F + \frac{d^2 F}{d\varsigma^2}. \tag{11}$$

Conservation of azimuthal momentum:

$$2FG + H \frac{dG}{d\varsigma} = \frac{\eta_p}{\omega r} G(\varsigma) \frac{1}{\rho} \frac{\partial P}{\partial r} + \frac{d^2 G}{d\varsigma^2}. \tag{12}$$

Conservation of axial momentum:

$$\omega \sqrt{\nu \omega} \left[H \frac{dH}{d\varsigma} - \frac{d^2 H}{d\varsigma^2} \right] = -g - \frac{1}{\rho} \frac{\partial P}{\partial z} + \frac{\eta_p}{\mu} \omega \sqrt{\nu \omega} H(\varsigma) \frac{\partial^2 P}{\partial \varsigma^2}. \tag{13}$$

Bödewadt neglected gravity and assumed that the pressure distribution above the ground plane boundary layer satisfied the rigidly rotating fluid column relation

$$\frac{1}{\rho} \frac{\partial P}{\partial r} = \omega^2 r, \tag{14}$$

invoking his boundary layer approximation to neglect axial variations in the pressure gradient. For the present non-equilibrium pressure case, we have examined the characteristic magnitude of the $\omega \sqrt{\omega \nu}$ prefix appearing in Eq. (13) for typical dust devil and tornado columnar rotation rates[10, 15, 19] (using a nominal kinematic viscosity for air of 1.5×10^{-5} m^2/s), and found that it ranged between 0.0005 m/s^2 and slightly less than 0.1 m/s^2. Consequently, a boundary layer approximation could be justified, but Schlichting's pressure correction procedure[18] can be employed to obtain an exact solution to the modified Navier-Stokes equations.

Since the geophysical problems of greatest interest include gravitational body forces, a modified version of Bödewadt's original pressure distribution function has been employed, incorporating the gravitational body force and introducing the required pressure correction function

$$P(r, z) = \rho \left[\frac{\omega^2 r^2}{2} - gz \right] + p'(\varsigma), \tag{15}$$

where $p'(\varsigma)$ must be evaluated after Eqs. (10)–(12) have been integrated numerically to obtain F, G, and $H(\varsigma)$. The equation governing the pressure correction function can thus be written

$$\frac{dp'}{d\varsigma} - \eta_p \omega H(\varsigma) \frac{d^2 p'}{d\varsigma^2} = \mu \omega \left[\frac{d^2 H}{d\varsigma^2} - H \frac{dH}{d\varsigma} \right]. \tag{16}$$

While it is possible to use standard integration techniques to represent the pressure correction function solution, i.e.,

$$p'(\varsigma) = \frac{\mu}{\eta_p} \int\limits_0^\varsigma H^{1/\eta_p\omega}(\tau) \int\limits_0^\tau H^{-1/\eta_p\omega}(\xi) \left[\frac{dH}{d\varsigma}(\xi) - \frac{1}{H} \frac{d^2H}{d\varsigma^2}(\xi) \right] d\xi \, d\tau, \tag{17}$$

the parametric values of $\eta_p\omega$ characterizing realistic geophysical flow structures were so small that integrating Eq. (17) may not be practical. Development of approximations to enable integration of Eq. (16) for very small values of $\eta_p\omega$ will be discussed for a dust devil example in Sec. IV A.

When the pressure distribution function, Eq. (15), is incorporated in the governing equations, the resulting radial and azimuthal conservation of momentum equations simplify to

$$F^2 + H\frac{dF}{d\varsigma} - G^2 + 1 = \eta_p\omega F + \frac{d^2F}{d\varsigma^2} \tag{18}$$

and

$$2FG + H\frac{dG}{d\varsigma} = \eta_p\omega G(\varsigma) + \frac{d^2G}{d\varsigma^2}. \tag{19}$$

It can be seen that when $\eta_p\omega = 0$, Eqs. (10), (18), and (19) revert to the system of equations employed in Bödewadt's original formulation.

The ground plane boundary conditions (no slip and no penetration) are straightforward, given by

$$F(0) = G(0) = H(0) = 0. \tag{20}$$

The far field boundary conditions at the top of the column were another matter when non-equilibrium pressure forces were included.[19] Classically, the boundary conditions at the top of the domain were assumed to apply in the infinite height limit.[17,18] The behavior of the azimuthal velocity component for the present "shielded," rotating fluid column far from the ground is still expected to revert to the rigid-body rotational behavior assumed by Bödewadt, i.e.,

$$\lim_{\varsigma \to \infty} G(\varsigma) = 1. \tag{21}$$

However, in the older formulation the radial velocity function, F, converged to zero and the axial velocity function, H, converged to a constant value of 1.3494, in the infinite limit.[18] That is not the case when non-equilibrium effects are included. From Eq. (19), it can be seen that if the rigidly rotating limit is achieved, and the derivatives of G go to zero, conservation of azimuthal momentum for large values of ς still requires that

$$\lim_{\varsigma \to \infty} 2FG(\varsigma) = \eta_p\omega \left[\lim_{\varsigma \to \infty} G(\varsigma) \right] = \eta_p\omega \Rightarrow F(\varsigma) \to \frac{\eta_p\omega}{2}, \tag{22}$$

indicating that radial flow persists for arbitrarily large values of ζ. That limit requirement also satisfies the conservation of radial momentum, Eq. (18), for large values of ς. In addition, the continuity equation, Eq. (10), must be satisfied and if

$$F(\varsigma) \to \frac{\eta_p\omega}{2}, \text{ for large values of } \varsigma,$$

then continuity requires that

$$\frac{dH}{d\varsigma}(\varsigma) \to -\eta_p\omega, \text{ for large values of } \varsigma. \tag{23}$$

In other words, the axial velocity component continues to decrease for arbitrarily large values of height, while the radial velocity component begins to vary linearly with radius. Both of these limiting requirements differ substantially from Bödewadt's original equilibrium solution. Not only does the radial velocity function cease to approach zero in the limit, but the limiting, negative slope of

the axial velocity function prevents the axial velocity from approaching a constant limiting value. Numerical integration of the radial and axial velocity functions for a range of $\eta_p\omega$, without imposing these upper limit conditions *a priori*, demonstrated that Eqs. (22) and (23) were correct. In addition, our parametric studies exhibited axial velocity functional behavior similar to Bödewadt's original equilibrium solution near the no-slip boundary, and the axial velocity function was always positive, prior to converging toward its theoretically predicted constant-negative-slope, and finally crossing zero.

It was possible to utilize the constant slope behavior at dimensionless heights well beyond Bödewadt's so-called boundary layer region[17] in order to determine the location where the axial velocity function passed through zero.[19] Since the axial velocity function always decreased linearly with height at large distances from the ground, our numerical studies[19] have shown that by incorporating non-equilibrium pressure gradient forces in the Navier-Stokes equations, the resulting ground-coupled solution was always bounded by a stagnation plane at a finite height (where $H(\varsigma_{\max}) = 0$).

Numerical results modeling dust devil behavior will be discussed as a particular case. In addition to dust devil profiles, we have examined characteristic angular rotation rates for tornadoes and cyclones, and utilized temperature and relative humidity data to estimate associated pressure relaxation coefficients. For all of the geophysical cases that have been examined, the magnitude of $\eta_p\omega$ was never larger than 0.00001, making it very difficult to capture solution details near the no-slip boundary. Those very small $\eta_p\omega$-values prevented direct integration of the pressure correction function using Eq. (17), and dimensionless column heights for those cases were so large that it was necessary to represent the functions using semi-log plots. Therefore, in order to observe the characteristic behavior of this type of rotating fluid column solution without requiring semi-logarithmic plots or utilizing additional approximations for the pressure correction function, a non-geophysical value of $\eta_p\omega = 0.1$, has been employed for discussion purposes. That parametric value could be relevant in modeling turbulent streak structures,[20,21] but it is an unrealistic geophysical scaling value.

The governing equations were integrated numerically out to arbitrarily large values of ς, in order to make sure that the finite lower domain (of unknown height) was traversed. A MathWorks, Inc. MATLAB *bvp4c* two-point boundary value solver was employed for the numerical integration of Eqs. (10), (18), and (19). That solver utilized Simpsons's method with residual control, implemented within an implicit fourth order Runge-Kutta formulation.[22] The extent of the required computational domain depended on the specified value of $\eta_p\omega$, and the upper stagnation-plane boundary had to be determined by trial and error. After the upper boundary was established, the final mesh for each $\eta_p\omega$ case was generated automatically utilizing a reverse interpolation strategy.

Variation of F, G, and $H(\varsigma)$, for Bödewadt's[17] original solution has been tabulated in Schlichting.[18] All three of the tabulated functions converged nominally to their limiting values for $\varsigma \approx 12.5$. A comparison between the Bödewadt functions (dashed lines) and the non-equilibrium functions (solid lines) for F, G, and $H(\varsigma)$, when $\eta_p\omega = 0.1$, is shown in Figures 1–3. Generally, the functional behavior near the ground for the "Bödewadt" and the non-equilibrium radial and azimuthal velocity functions have similar shapes, except the non-equilibrium radial velocity function (Figure 1) can be observed to converge toward a limiting value of 0.05 rather than zero, while the azimuthal velocity function (Figure 2) appears to exhibit more damping when non-equilibrium pressure forces are included, converging more rapidly toward unity. Away from the ground, the axial velocity function (Figure 3) appears to have been "bent" from its original constant-height limit [where $H(\varsigma) \to 1.3494$], into a limiting straight line with a slope of -0.1, crossing zero at $\varsigma = 14.17$. As was the case for the azimuthal velocity function, the oscillatory behavior of the axial velocity function near the ground appears to be damped by the non-equilibrium pressure forces.

Regardless of the specified value of $\eta_p\omega$, the numerical integration limits could be extended well beyond the height where the vertical velocity component was equal to zero. Hence, the fluid region above the stagnation plane boundary could also be examined.[19] Streamlines in the unbounded upper region represented a type of downward-flowing stagnation flow, and the upper flow domain had many of the characteristics of a boundary layer flow produced by a rotating disk beneath a quiescent fluid.[18] The upper solution domain provides a link between upper atmospheric flow
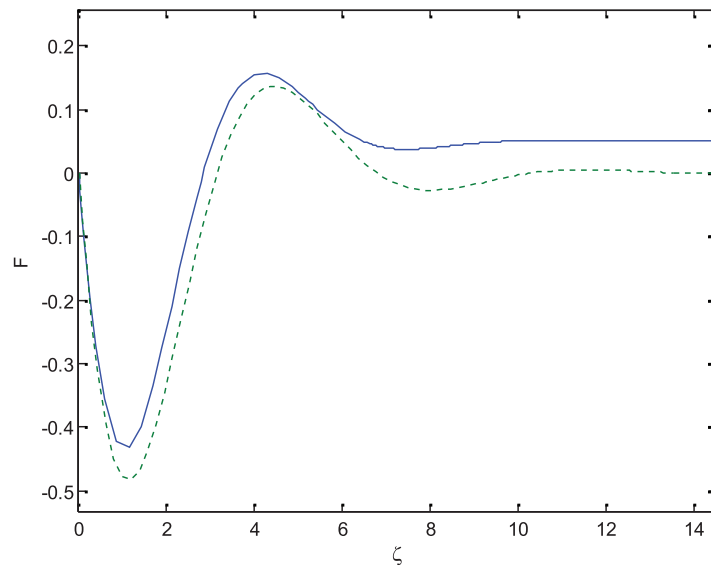
FIG. 1. Comparison of the radial velocity distribution function representing a pressure relaxation parameter, $\omega\eta_p$, equal to 0.1 (solid line), with Bödewadt's solution[17, 18] (dashed line).

behavior and the lower, rotating-column flow unit, but for present purposes, the upper domain has been ignored.

A. Pressure correction function

The pressure correction function, given by Eq. (17), was integrated numerically for the $\eta_p\omega = 0.1$ case[24] and is displayed in Figure 4. The pressure correction function is quite small compared with the predicted pressure deficit. Maximum pressure correction adjustments near the ground plane boundary were less than 2% of the maximum far-field pressure deficit. The pressure
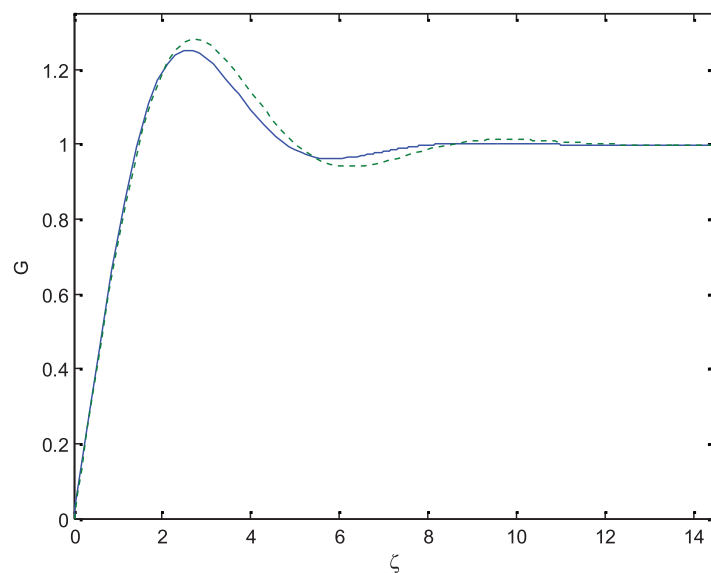

FIG. 2. Comparison of the azimuthal velocity distribution function representing a pressure relaxation parameter, $\omega\eta_p$, equal to 0.1 (solid line), with Bödewadt's solution[17, 18] (dashed line).
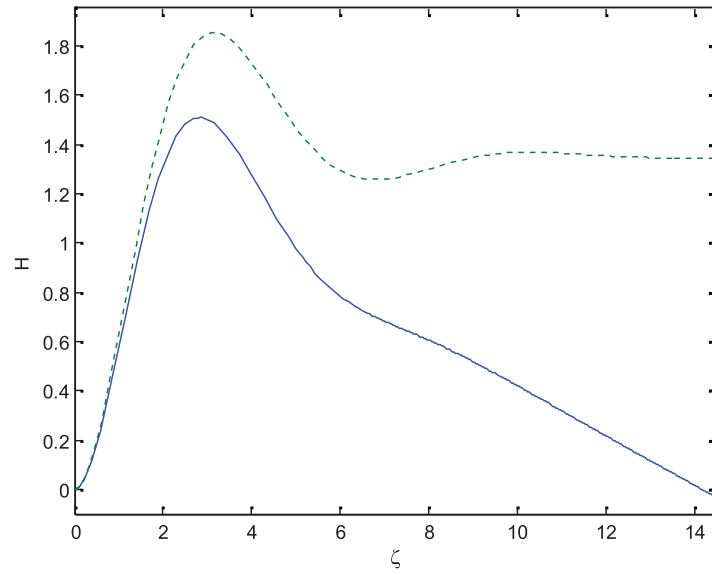
FIG. 3. Comparison of the axial velocity distribution function representing a pressure relaxation parameter, $\omega\eta_p$, equal to 0.1 (solid line), with Bödewadt's solution[17,18] (dashed line).

correction was -0.13% of the maximum pressure deficit at the location where the axial velocity was equal to zero.

After numerical integration established the ς-location where the axial velocity went to zero [designated as $\varsigma_{\max}(\eta_p\omega)$, since it was a function of $\eta_p\omega$], the height of the ground-coupled flow domain was

$$h_{\max} = \sqrt{\frac{\nu}{\omega}}\,\varsigma_{\max}\left(\eta_p\omega\right), \tag{24}$$

and the associated boundary conditions on that boundary were
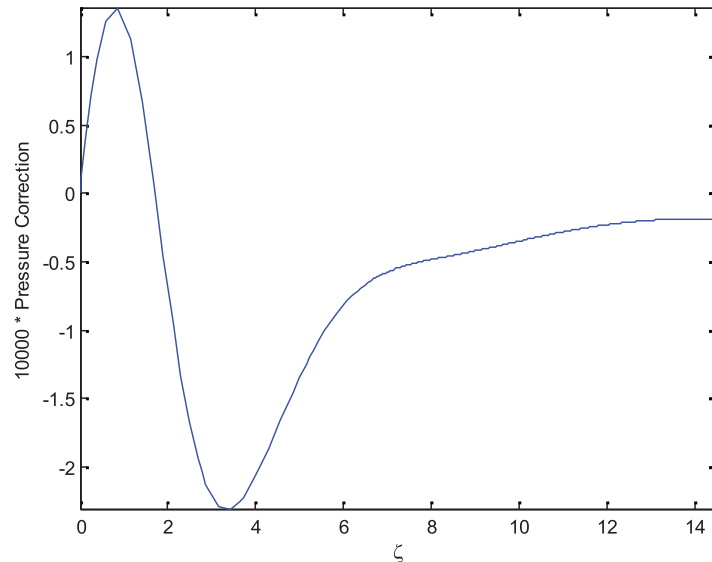
$$v_z\left(r, h_{\max}\right) = 0, \tag{25}$$

FIG. 4. Variation of the pressure correction function with dimensionless height: $\omega\eta_p = 0.1$.

$$v_r \left(r, h_{\max} \right) = \frac{\eta_p}{2} \omega^2 r, \tag{26}$$

$$v_\theta \left(r, h_{\max} \right) = \omega r, \tag{27}$$

and

$$P \left(r, h_{\max} \right) = \rho \left[\frac{\omega^2 r^2}{2} - g\, h_{\max} \right] + p' \left(\varsigma_{\max} \right). \tag{28}$$

The three normal stress components along the top boundary are given by

$$\sigma_r \left(r, h_{\max} \right) = \mu \eta_p \omega^2 = \sigma_\theta \left(r, h_{\max} \right) = -\frac{1}{2} \sigma_z \left(r, h_{\max} \right), \tag{29}$$

and the three shear stresses were equal to zero at the boundary, i.e.,

$$\tau_{r\theta} \left(r, h_{\max} \right) = \tau_{rz} \left(r, h_{\max} \right) = \tau_{\theta z_z} \left(r, h_{\max} \right) = 0. \tag{30}$$

Hence, there are no shear stresses acting at the top of the finite-height, rotating fluid column, but the surface traction force exerted on the stagnation plane is

$$\frac{F_{Normal}}{A} \left(r, h_{\max} \right) = -P \left(r, h_{\max} \right) + \sigma_z \left(r, h_{\max} \right) = -P \left(r, h_{\max} \right) - 2\mu \eta_p \omega^2, \tag{31}$$

where surface traction forces are considered to be positive in tension.

The surface traction force along the top boundary has been employed to control the constant of integration in the pressure correction function. That is, if the finite column height represents the extent of the domain in which non-equilibrium pressure forces are operative, then it is logical to require that the surface traction force reverts to the equilibrium pressure distribution along the stagnation plane, i.e.,

$$\frac{F_{Normal}}{A} \left(r, h_{\max} \right) = -\rho \left[\frac{\omega^2 r^2}{2} - g\, h_{\max} \right] = -\rho \left[\frac{\omega^2 r^2}{2} - g\, h_{\max} \right] - p' \left(\varsigma_{\max} \right) - 2\mu \eta_p \omega^2.$$

On that basis, we require that

$$p' \left(\varsigma_{\max} \right) = -2\mu \eta_p \omega^2. \tag{32}$$

In the numerical example ($\eta_p \omega = 0.1$), the integrated value of the pressure correction function at the top of the domain was -0.0013 Pa, which represented $\Delta p' = p'(\varsigma_{\max}) - p'(0)$. By employing an initial value, $p'(0) = 0.0037$ Pa, Eq. (32) was satisfied and the pressure at the top of the domain then coincided with the equilibrium pressure for a rotating fluid column.

B. Estimation of fluid column height

The range of expected values of $\eta_p \omega$ for geophysical cyclonic flows required specification of both the pressure relaxation coefficient and the angular rotation rate of actual cyclones. Currently, pressure relaxation coefficients for air can only be inferred utilizing acoustic reference data.[14] Those acoustically based estimates demonstrate that the pressure relaxation coefficient can vary by more than two orders of magnitude at a given ambient temperature, depending on relative humidity. Tornadoes and hurricanes are much more complicated than are dust devils because of multi-phase water transport processes along with cloud and frontal weather dynamics, to say nothing of their overall size. In addition, the high levels of humidity associated with those types of cyclonic flows result in substantially smaller values of η_p, and therefore smaller values of $\eta_p \omega$. Consequently, the largest value of $\eta_p \omega$, estimated for a low-humidity dust devil,[19] was approximately 0.00001, and the heights of all of these rotating fluid columns can be expected to be associated with $\eta_p \omega \leq 0.00001$. For the high-moisture-content columnar rotation that would characterize tornadoes and cyclones,

$\eta_p\omega$ is expected to be much smaller. Numerical experiments over a wide range of $\eta_p\omega$ demonstrated that it was possible to predict the maximum column height quite accurately using the empirical curve-fit relation,

$$h_{\mathrm{max}} = \frac{1.394}{\eta_p\omega}\sqrt{\frac{\nu}{\omega}}. \tag{33}$$

Based on the earlier axial vortex study,[15] turbulence could be taken into account by utilizing a turbulent eddy viscosity, ν_{turb}, in place of the fluid transport property. Thus, the maximum height of these rotating fluid columns varied directly with the square root of kinematic (or eddy) viscosity and inversely with the pressure relaxation coefficient and with the 3/2 power of the angular rotation rate. The more turbulent the central core, the taller the column; the drier the air (the larger the value of the pressure relaxation coefficient) or the faster the rotation rate, the shorter the column.

## IV. ESTIMATION OF CENTRAL COLUMN HEIGHTS OF DUST DEVILS

Dust devil data were used to test the applicability of Eq. (33). Hess and Spillane[23] compiled statistical data for 26 dust devils observed by general aviation pilots in Australia between November 1, 1987 and January 31, 1988; they also noted that visible dust devil column heights as tall as 2400 m had been reported by others. Out of 26 dust devil observations, 18 multiple dust devil observation sets were compiled, along with eight single dust devil height observations. The mean observed dust devil heights were 661 m for the 18 multiple dust devil events and 402 m for the eight single-event dust devils, with standard deviations of 179 m and 142 m, respectively. Since the pilot observations were made remotely with respect to the dust devil positions, the local ambient temperature, pressure, and relative humidity characterizing each dust devil was unknown, precluding direct use of those observations in the present theory. On the other hand, Sinclair[10] reported detailed structural measurements of three dust devils that were encountered near Tucson, Arizona between August 7 and 14, 1962; unfortunately, they did not measure the local relative humidity or the actual heights of the encountered dust devils. However, the relative humidity could be estimated for the Sinclair dust devils using nominal hour-by-hour dew point data measured at the nearby Tucson, AZ weather station.[15] The three dust devils were turbulent and in our previous study, we discussed how it was possible to employ the measured dust devil core diameters and maximum rotational velocities to estimate appropriate turbulent eddy viscosities.[15] Using the measured local ambient temperature, pressure, and core rotational velocity, along with the estimated dew point temperature, the dry-air pressure relaxation coefficients could be predicted theoretically.[14] Then, employing the turbulent eddy viscosities estimated from our earlier study, it was possible to utilize the structural characteristics of Sinclair's three dust devils, as summarized in Table I, in Eq. (33) to estimate the height of each rotating dust devil column. If dust devil DD #3 (observed on August 14, 1962) was part of a multiple dust devil event, its substantially different structural characteristics and estimated column height are consistent with the multiple-event statistics of Hess and Spillane.[23] The first two dust devils had estimated column heights that were within one standard deviation of Hess and Spillane's average single-event height estimates.

TABLE I. Structural properties of the Sinclair[10,15] dust devils, along with estimated column heights.[19]

Dust devil	η_p (μs)	r_{core} (m)	v_{max} (m/s)	ω_{core} (s^{-1})	ν_{eff} (m^2/s)	Estimated stagnation height (m), Eq. (33)
DD #1	1.049	2.3	11	9.6	7.1×10^{-5}	378
DD #2	1.125	2.6	12	9.24	7.1×10^{-5}	357
DD #3	1.092	3.35	8.8	5.25	6.2×10^{-5}	833

A. Velocity and pressure distributions in the central column of Dust Devil #1[10]

From Table I, Sinclair's Dust Devil #1 represented the largest nominal value for $\omega\eta_p$ (equal to 0.00001). The predicted maximum dimensionless height for a rotating central fluid column representative of Sinclair's Dust Devil #1, was 139 000, corresponding to a physical column height of 378 m. Due to the extremely large extent of the dimensionless flow domain, the overall dimensionless functional behavior of the radial, azimuthal, and axial velocity functions masked the local variations near the solid boundary. Hence, the dimensionless plots of the radial, azimuthal, and axial velocity functions for that rotating fluid column are shown as semi-log overall plots (panels (a)) and linear, near-the-ground plots (panels (b)) in Figures 5–7. In that way, the overall and near-surface behavior can be observed. From these figures, it can be seen that the dimensionless variations of the velocity functions near the ground boundary for that dust devil column
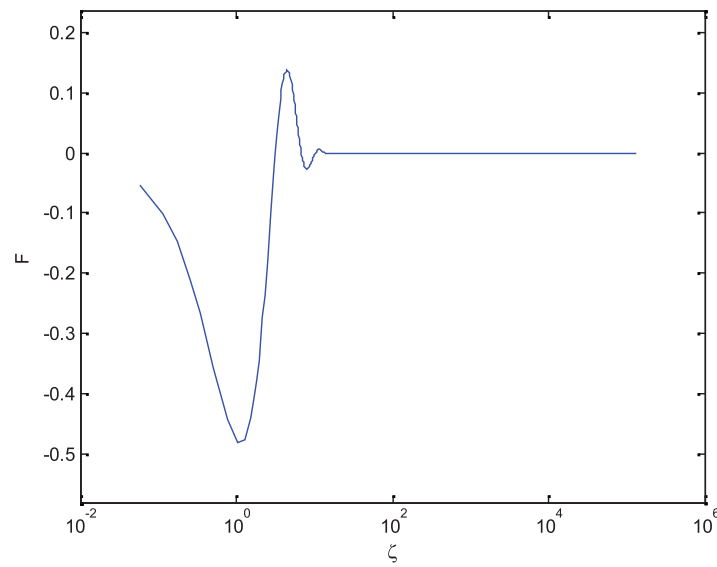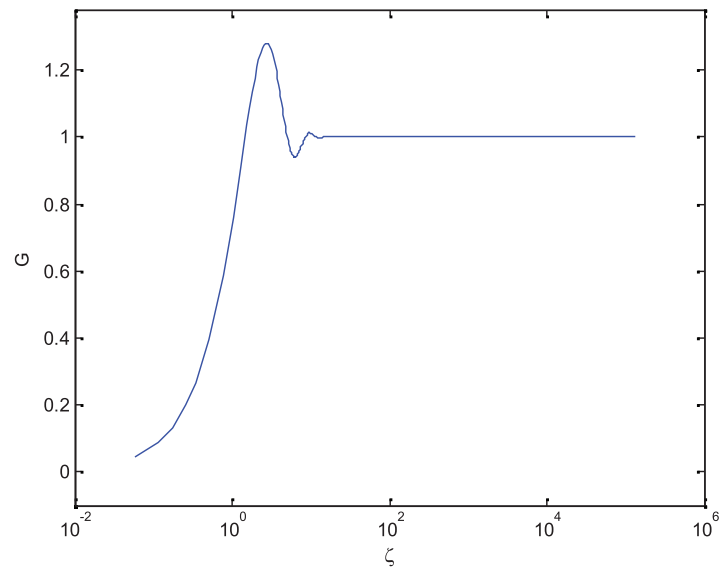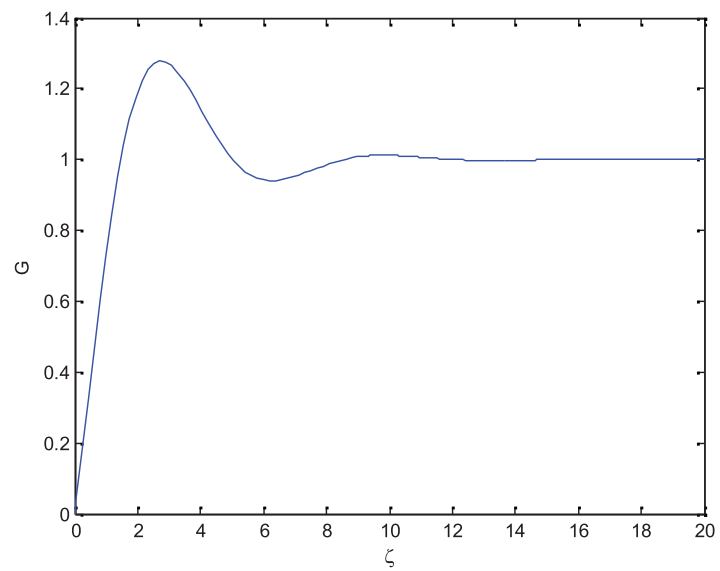

(a)
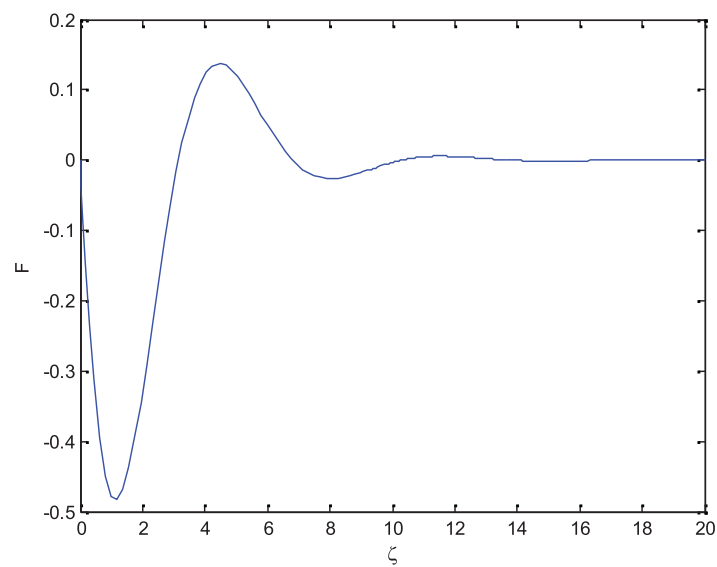
(b)

FIG. 5. Variation of the radial velocity function with ζ, for $\omega\eta_p = 0.00001$ (a) $\zeta_{max} = 139\,000$ and (b) near the ground plane.
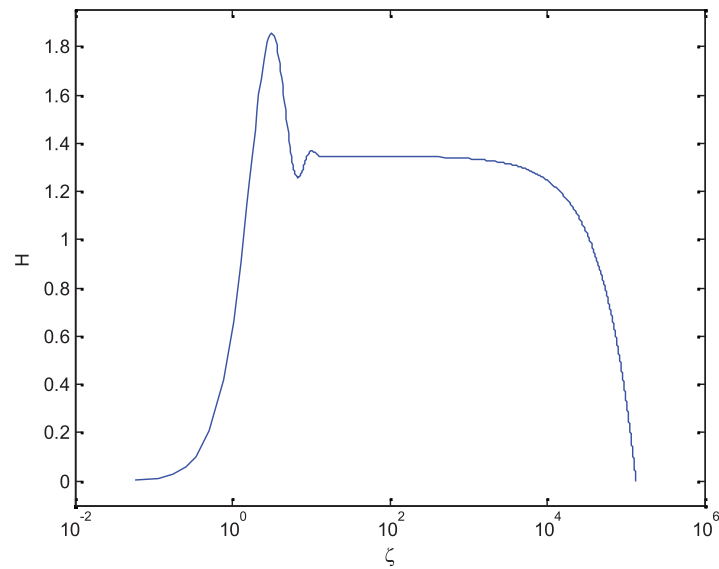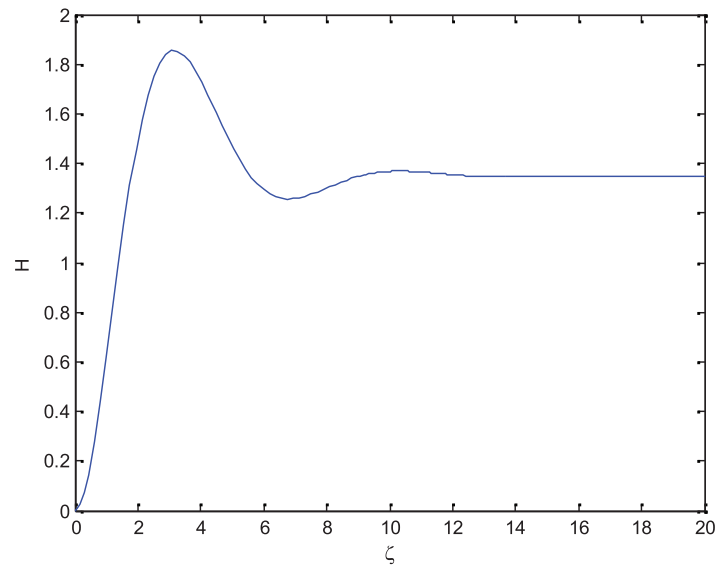
(a)

(b)

FIG. 6. Variation of the azimuthal velocity function with ζ, for $\omega\eta_p = 0.00001$ (a) $\zeta_{max} = 139\,000$ and (b) near the ground plane.

(a)

(b)

FIG. 7. Variation of the axial velocity function with ζ, for $\omega\eta_p = 0.00001$ (a) $\zeta_{max} = 139\,000$ and (b) near the ground plane.

are nearly identical with the velocity functions for the non-physical $\omega\eta_p = 0.1$ case. The primary difference is the extremely slow decrease in the dimensionless axial velocity function, when $\omega\eta_p = 0.00001$.

The $\omega\eta_p = 0.00001$ case represents a type of upper limit for estimating the non-equilibrium pressure correction effects in a geophysical vortex (other cases will be even smaller). Examination of the closed integral solution for the pressure correction function given by Eq. (17), and utilized for the demonstration case shows that it would require raising numerically integrated functions to powers of $\pm 100\,000$, in this case and any realistic numerical resolution and accuracy specification cannot support such calculations, requiring an alternate numerical integration approach.

The dynamic viscosity for air using the ambient conditions for DD #1 was 0.000019 Pa s. Employing the data from Table I, the pressure correction function equation, Eq. (16), could be written

$$\frac{dp'}{d\varsigma} = \mu\omega \left[\frac{d^2H}{d\varsigma^2} - H\frac{dH}{d\varsigma}\right] + \omega\eta_p H(\varsigma)\frac{d^2p'}{d\varsigma^2}$$

$$= 0.000184 \left[\frac{d^2H}{d\varsigma^2} - H\frac{dH}{d\varsigma}\right] + 0.00001 H(\varsigma)\frac{d^2p'}{d\varsigma^2} \tag{34}$$

for this case. From the conservation of axial momentum equation, the initial slope of the pressure correction function is given by

$$\frac{dp'}{d\varsigma}(0) = -\omega\mu\frac{d^2H}{d\varsigma^2}(0) = 2\omega\mu\frac{dF}{d\varsigma}(0) = 0.000368\frac{dF}{d\varsigma}(0). \tag{35}$$

Near the ground plane, Eq. (34) was integrated iteratively by first neglecting the second derivative pressure correction term, and subsequently utilizing the numerically predicted pressure correction function from the previous iteration to calculate the second derivative of the pressure correction, repeating the process until acceptable accuracy was achieved.

Iteration effects were only detectable in the vicinity of the ground boundary. Since $\frac{dH}{d\varsigma} = -2F(\varsigma)$, from Eq. (10), Figure 5(b) shows that the numerically integrated values of $F(\varsigma)$ have converged to the limiting constant value, $\frac{\omega\eta_P}{2}$, well before $\varsigma = 100$. Therefore, the axial velocity function varied linearly with ς thereafter, and $\frac{dH}{d\varsigma} = -\omega\eta_p = $ constant, for $\varsigma \geq \varsigma_{crit}$, to acceptable accuracy. When the axial velocity function could be approximated as a linear function of height, the second derivative of H could be neglected, and the term in braces in Eq. (34) could be approximated:

$$\mu\omega \left[H\frac{dH}{d\varsigma} - \frac{d^2H}{d\varsigma^2}\right] \approx \frac{\mu\omega}{2}\frac{d}{d\varsigma}\left(H^2\right). \tag{36}$$

Also,

$$\frac{dp'}{d\varsigma} - \eta_p\omega H(\varsigma)\frac{d^2p'}{d\varsigma^2} = \frac{d}{d\varsigma}\left[p' - \eta_p\omega H(\varsigma)\frac{dp'}{d\varsigma}\right] + \eta_p\omega\frac{dH}{d\varsigma}\frac{dp'}{d\varsigma}$$

$$\approx \frac{d}{d\varsigma}\left[p' - \eta_p\omega H(\varsigma)\frac{dp'}{d\varsigma}\right] - (\eta_p\omega)^2\frac{dp'}{d\varsigma} = \eta_p\omega\frac{d}{d\varsigma}\left[\left(\frac{1}{\eta_p\omega} - \eta_p\omega\right)p' - H(\varsigma)\frac{dp'}{d\varsigma}\right].$$

Hence,

$$\frac{\mu}{2\eta_p}\frac{d}{d\varsigma}\left(H^2\right) = \frac{d}{d\varsigma}\left[\left(H\frac{dp'}{d\varsigma}\right) + \left(\omega\eta_p - \frac{1}{\omega\eta_p}\right)p'\right], \text{ for } \varsigma \geq \varsigma_{crit}. \tag{37}$$

Then, integrating between the minimum linear slope approximation height, ς_{crit}, and ς,

$$\frac{\mu}{2\eta_p}\left[H^2(\varsigma) - H^2(\varsigma_{crit})\right] = H(\varsigma)\frac{dp'}{d\varsigma}(\varsigma) - H(\varsigma_{crit})\frac{dp'}{d\varsigma}(\varsigma_{crit})$$

$$- \left(\frac{1}{\omega\eta_p} - \omega\eta_p\right)\left[p'(\varsigma) - p'(\varsigma_{crit})\right]$$

or

$$H(\varsigma)\frac{dp'}{d\varsigma}(\varsigma) - \left(\frac{1}{\omega\eta_p} - \omega\eta_p\right)p'(\varsigma) = \frac{d}{d\varsigma}\left[H\,p'\right] - \left(\frac{1}{\omega\eta_p} - 2\omega\eta_p\right)p'(\varsigma)$$

$$= \frac{\mu}{2\eta_p}H^2(\varsigma) + H(\varsigma_{crit})\frac{dp'}{d\varsigma}(\varsigma_{crit}) - \frac{\mu}{2\eta_p}H^2(\varsigma_{crit}) - \left(\frac{1}{\omega\eta_p} - \omega\eta_p\right)p'(\varsigma_{crit}).$$

Finally, since $\omega\eta_p \ll 1$, this differential equation could be simplified further as

$$\omega\eta_p \frac{d}{d\varsigma}\left[H\,p'\right] - p'(\varsigma) = \frac{\mu\omega}{2}H^2(\varsigma) + \omega\eta_p H(\varsigma_{crit})\frac{dp'}{d\varsigma}(\varsigma_{crit}) - \frac{\mu\omega}{2}H^2(\varsigma_{crit}) - p'(\varsigma_{crit})$$

$$\Rightarrow p'(\varsigma) \approx p'(\varsigma_{crit}) - \frac{\mu\omega}{2}\left[H^2(\varsigma) - H^2(\varsigma_{crit})\right], \quad \text{for} \quad \varsigma \geq \varsigma_{crit}. \tag{38}$$
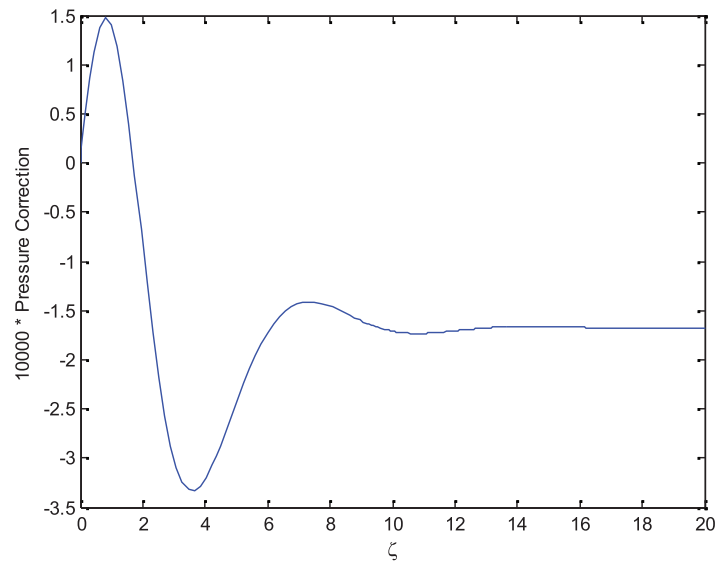
Also, since $H(\varsigma_{\max}) = 0$, the pressure correction at the top of the domain is given by

$$p'(\varsigma_{\max}) = p'(\varsigma_{crit}) + \frac{\omega\mu}{2}H^2(\varsigma_{crit}). \tag{39}$$

The overall pressure correction function, employing iteration and these additional approximations, is shown in Figure 8(a), while its variation in the vicinity of the ground plane boundary is shown in
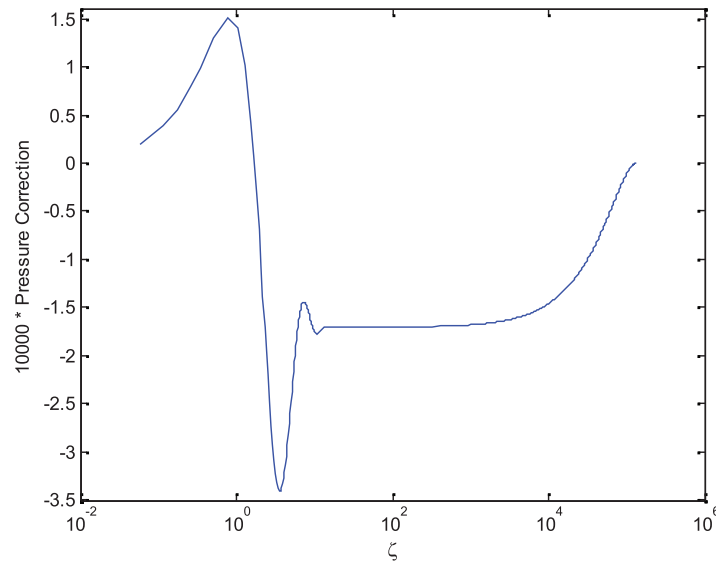
(a)

(b)

FIG. 8. Variation of the pressure correction function with ζ: $\omega\eta_p = 0.00001$ (a) $\zeta_{max} = 139\,000$ and (b) near the ground.
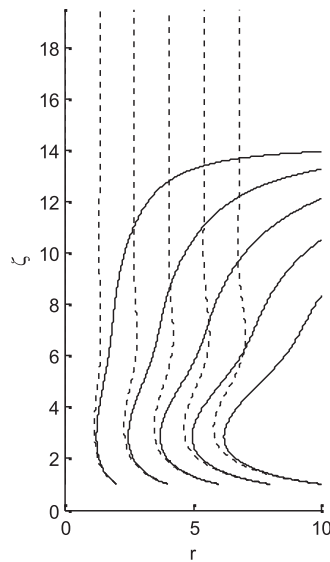
FIG. 9. Comparison between two-dimensional streamline patterns representing pressure relaxation parameter solution, $\omega\eta_p = 0.1$ (solid line), and Bödewadt's solution[17, 18] (dashed line).

Figure 8(b). The behavior near the ground plane is very similar to the directly integrated behavior for the case when $\omega\eta_p = 0.1$, while the pressure correction away from the ground appears to have simply been "stretched" over a very large dimensionless distance.

V. RESULTS AND DISCUSSION

The importance of incorporating non-equilibrium pressure forces in this rotating fluid column model can be demonstrated most easily by comparing streamline behavior for the classical solution with the streamline patterns for the two non-equilibrium pressure examples, as shown in Figures 9–11. Figure 9 shows that in the immediate vicinity of the ground plane, fluid particles
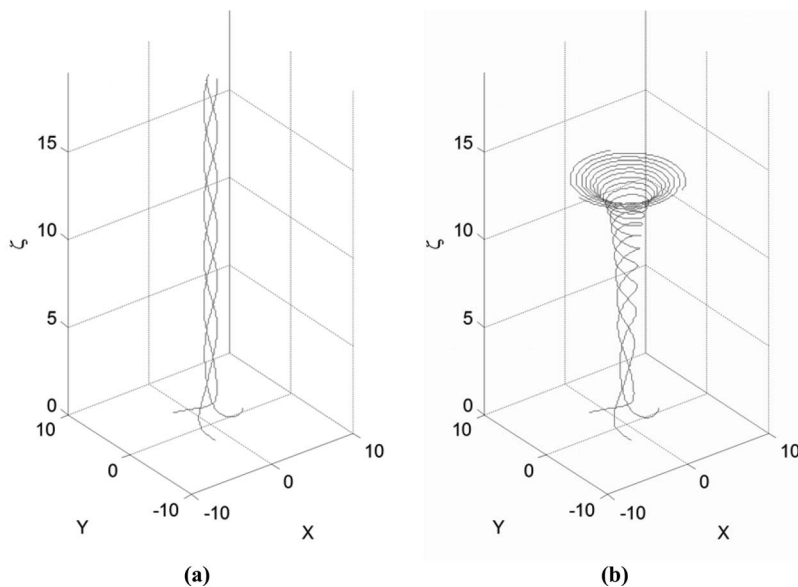

FIG. 10. Three-dimensional streamline patterns. (a) Bödewadt's solution.[17, 18] (b) Present solution, $\omega\eta_p = 0.1$.
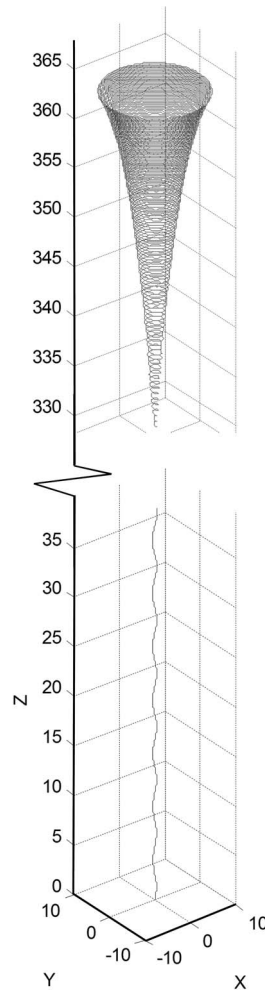
FIG. 11. Three-dimensional streamline patterns for $\omega\eta_p = 0.00001$ (dimensions in meters).

are drawn toward the rotational axis in the same manner as the classical solution and the influence of non-equilibrium pressure effects is virtually undetectable. However, at dimensionless heights greater than 2, the gradual retardation of the vertical component of velocity by the non-equilibrium pressure forces causes the particle trajectories (solid lines) to begin to diverge from the rotational axis. The streamlines become parallel to the ground plane at a dimensionless height of 14.17. The three-dimensional representations of four "corkscrew" streamlines representing the original Bödewadt solution,[17, 18] shown in Figure 10(a), demonstrate that those streamlines have constant nominal pitches of one rotation per 5 m, extending to infinity. Conversely, Figure 10(b) shows how the non-equilibrium pressure forces acting on four streamlines, initiated at the same nominal ground plane locations as the streamlines in Figure 10(a), become "trapped" below a dimensionless height of 14.17. Those streamlines generate a funnel shape.

For the $\omega\eta_p = 0.00001$ case, which is representative of a dust devil column, the extremely slow retardation of the vertical velocity component, results in a very slow corresponding increase in the radial component of the velocity. Figure 11 is a plot of a single streamline for that case, started near the ground plane at an initial radius of 0.3 m. The vertical scale (in meters) is broken because the change in corkscrew pitch, and the corresponding gradual dilation of the streamline is barely detectable over substantial vertical distances, until the particle path is near the top of the column. As can be seen in the figure, at a height of 330 m, the helical pitch is approximately three rotations per meter, compared to an initial pitch, near the ground plane, of approximately 0.2 revolutions per

meter. At the vertical upper limit, the pitch will be infinite, since the vertical velocity goes to zero, but it is not possible to show that part of the streamline (out to 378 m), since that depiction takes on the appearance of a picture from a coloring book.

The pressure correction function also yields an estimate of the surface pressure gradient beneath the rotating fluid column. That is,

$$\frac{\partial P}{\partial z}(r, 0) = -\rho g + 2\mu \frac{\omega^{3/2}}{\nu} \frac{dF}{d\varsigma}(0),\tag{40}$$

beneath the rotating column, where the turbulent eddy viscosity from Table I, is employed for the present Dust Devil #1 case. For that dust devil, the rotating column contribution to the estimated surface pressure gradient [with $\frac{dF}{d\varsigma}(0) = -0.942$] is -0.128 Pa/m, corresponding to slightly more than a 1% increase in the surface pressure gradient.

VI. CONCLUSIONS

This work has shown that non-equilibrium pressure gradient forces, when incorporated in a model of a ground-coupled, rotating fluid column, provide a mechanism for controlling the height of the column. Employing data from an earlier analysis of dust devils,[15] the present model has shown that the estimated central column heights utilizing the present theory for three dust devils whose near-surface environmental and structural characteristics had been measured previously by Sinclair,[10] were consistent with the statistically based dust devil heights cataloged by Hess and Spillane.[23] This research therefore supports de-constructing geophysical axial vortex structures into distinguishable zones, like the layers of a chive, separating the inner "rigidly rotating" fluid column layer from the intermediate non-equilibrium transitional flow layer and finally from the outer potential vortex "layer," for modeling purposes. If the rotating fluid column region is shielded from the outer flow, ground coupling tends to preserve the rotating column flow unit by drawing in additional fluid near the ground. When non-equilibrium pressure gradient forces are included, the ground-coupled, rotating central fluid column is constrained to a finite height because the non-equilibrium pressure forces retard the vertical upward flow. Conservation of mass demands that the radial component of velocity increase with height in order to accommodate the fluid that would otherwise accumulate because of the decelerating vertical flow. The simultaneous variation of the vertical and radial velocity components with height results in funnel-shaped streamlines. In contrast with the bottom boundary, the expanding streamlines near the top dilate the column and impose constraints on the outer potential vortex region of the flow.

At the top of the rotating column, the pressure correction function can be utilized to impose the equilibrium pressure distribution produced by a rigidly rotating fluid column under the influence of gravity. Since the shear stresses produced at the top of this finite fluid column are equal to zero, the exact solution to the modified Navier-Stokes equations for the finite fluid column which results can exist beneath the complimentary upper stagnation layer flow.[19] Unlike the in-flow conditions near the ground plane boundary, the expanding top of the rotating column must alter the outer flow regime, placing limits on the extent of the multiple layer representation.

The dimensionless pressure relaxation parameter, $\omega\eta_p$, characterizing observed dust devil and tornado flows was found to be very small. However, when pressure relaxation parameters were estimated for the three dust devils that had been documented in some detail by Sinclair,[10] the estimated heights were found to be consistent with dust devil height statistical data. A numerical investigation of the velocity, pressure, and streamline patterns representing Sinclair's Dust Devil #1 showed that ground coupling resulted in a central, rotating fluid column streamline pattern that was nearly identical with the corkscrew pattern predicted by Bödewadt,[17] over approximately 80% of the bottom region. However, above that height the funnel shaped streamlines became pronounced. In addition, the exact pressure distribution solution predicts that a small, non-equilibrium-derived pressure gradient is produced along the ground plane that enhances particle levitation.

[1] R. Fernandez-Feria and J. C. Arrese, "Boundary layer induced by a conical vortex," Q. J. Mech. Appl. Math. **53**, 609 (2000).
[2] L. Parras and R. Fernandez-Feria, "Interaction of an unconfined vortex with a solid surface," Phys. Fluids **19**, 067104 (2007).
[3] R. R. Long, "A vortex in an infinite fluid," J. Fluid Mech. **11**, 611 (1961).
[4] R. L. Ash and M. R. Khorrami, "Vortex Stability," in *Fluid Vortices*, edited by S. I. Green (Kluwar Academic Publishers, Dordrecht, The Netherlands, 1995), Chap. VIII, Vol. 317.
[5] N. B. Ward, "The exploration of certain features of tornado dynamics using a laboratory model," J. Atmos. Sci. **29**, 1194 (1972).
[6] C. R. Church and J. T. Snow, "The dynamics of natural tornadoes as inferred from laboratory simulations," J. Rech. Atmos. **12**, 111 (1979).
[7] W. R. C. Phillips, "On vortex boundary layers," Proc. R. Soc. London, Ser. A **400**, 253 (1985).
[8] W. R. C. Phillips and B. C. Khoo, "The boundary layer beneath a Rankine-like vortex," Proc. R. Soc. London, Ser. A **411**, 177 (1987).
[9] A. Hirsa, J. M. Lopez, and S. Kim, "Evolution of an initially columnar vortex terminating normal to a no-slip wall," Exp. Fluids **29**, 309 (2000).
[10] P. C. Sinclair, "The lower structure of dust devils," J. Atmos. Sci. **30**, 1599 (1973).
[11] W. H. Hoecker, Jr., "Wind speed and air flow patterns in the Dallas Tornado of April 2, 1957," Mon. Weather Rev. **88**, 167 (1960).
[12] W. J. M. Rankine, *A Manual of Applied Mechanics*, 5th ed. (Charles Griffin and Co., London, 1869).
[13] A. J. Zuckerwar and R. L. Ash, "Variational approach to the volume viscosity of fluids," Phys. Fluids **18**, 047101 (2006).
[14] A. J. Zuckerwar and R. L. Ash, "Volume viscosity in fluids with multiple dissipative processes," Phys. Fluids **21**, 033105 (2009).
[15] R. L. Ash, I. Zardadkhan, and A. J. Zuckerwar, "The influence of pressure relaxation on the structure of an axial vortex," Phys. Fluids **23**, 073101 (2011).
[16] C. C. Lim, "Phase transition to super-rotating atmospheres in a simple planetary model for a nonrotating massive planet: Exact solution," Phys. Rev. E **86**, 066304 (2012).
[17] U. T. Bödewadt, "Die Drehströmung über festem Grunde," Z. Angew. Math. Mech. **20**(5), 241 (1940).
[18] H. Schlichting, *Boundary Layer Theory*, 7th ed. (McGraw Hill, New York, 1979).
[19] I. R. Zardadkhan, "The influence of non-equilibrium pressure on rotating flows," Ph.D. dissertation (Mechanical and Aerospace Engineering Department, Old Dominion University, May 2012).
[20] R. Monchaux, F. Ravelet, B. Dubrulle, A. Chiffaudel, and F. Daviaud, "Properties of steady states in turbulent axisymmetric flows," Phys. Rev. Lett. **96**, 124502 (2006).
[21] R. J. Adrian, "Hairpin vortex organization and wall turbulence," Phys. Fluids **19**, 041301 (2007).
[22] J. Kierzenka and L. F. Shampine, "A BVP solver based on residual control and the MATLAB PSE," ACM Trans. Math. Softw. **27**, 299 (2001).
[23] G. D. Hess and K. T. Spillane, "Characteristics of dust devils in Australia," J. Appl. Met. **29**, 498 (1990).
[24] In order to integrate the pressure correction function for this unrealistic case, the following conditions were assumed: very dry air at $50\,^\circ$C and 1 atm, with a pressure relaxation coefficient of 80 μs, a core angular rotation rate of 1250 rad/s and a kinematic viscosity of 1.8×10^{-5} m^2/s, resulting in a core radius of 1 mm, and an estimated maximum pressure deficit of 1 Pa, away from the ground (with a nominal rotating central column diameter of 0.2 mm). The estimated height of such a rotating air column was 1.7 mm.